Modeling Dynamics of Agile Fixed-Wing UAVs for Real-Time Applications

Waqas Khan and Meyer Nahon, *Senior Member, IEEE*

Abstract— A special class of fixed-wing UAVs called agile UAVs have emerged recently, that are lightweight with control surfaces as big as 50% chord capable of deflecting up to 50 deg., and are characterized by high thrust-to-weight ratios of around 2-3, and a strong propwash. Such configuration allows agile UAVs to perform extreme aerobatic maneuvers that expand the conventional flight envelope to cover the full angle of attack and sideslip range. The desire to automate these aerobatic capabilities has led to a renewed interest in fixed-wing UAVs with a focus on understanding and modeling their dynamics for the full flight envelope. This paper presents a six degree-of-freedom dynamics model for agile UAVs obtained through first principles. Simple but accurate techniques are presented to model the aerodynamics, thruster dynamics and propeller slipstream effects, which are embedded into the overall UAV simulation that is setup to run both offline as well as in real-time with the pilot-in-loop. Static bench tests are performed for validation of the presented six-dof agile UAV model and underlying modeling techniques. As well, qualitative validation shows the model to successfully capture well-known RC maneuvers flown by an experienced pilot in real-time simulation.

Figure 1. An agile fixed-wing UAV performing aerobatics.

I. INTRODUCTION

Agile UAVs, owing to their low weight and inertia, control surfaces as big as 50% chord, large deflections up to 50 deg., and powerful thrusters producing high thrust-to-weight ratios of around 2, and a strong slipstream, attain maneuverability paralleling that of rotorcraft and flapping-wing UAVs, while retaining their capability of long-distance flight. As such, agile UAVs exploit both the efficient cruise flight of fixed-wing UAVs and the maneuvering capabilities of rotorcraft and flapping-wing UAVs.

Remote control (RC) pilots routinely perform impressive aerobatic feats with small fixed-wing RC planes that fall in the category of agile UAVs (see Fig. 1). The desire to mimic these capabilities autonomously has led to a renewed interest in fixed-wing UAVs with a focus on understanding and modeling their dynamics for the full flight envelope i.e. complete ± 180 deg. angle of attack and sideslip range. Realization of such autonomous capabilities will make them the ideal aerial platform for a broad spectrum of applications including flight in constrained environments and limited spaces such as indoors, caves etc., flight that require rapid maneuvers like evasion, perching, stop and stare etc., and in general, applications that require a long transit before executing specified maneuvers at the target destination.

Whereas conventional flight of fixed-wing UAVs have been studied for quite long now and have become a standard textbook topic, the behavior of agile fixed-wing UAVs is not well understood and remains largely a challenge till today. The flight dynamics of agile UAVs are quite different from conventional fixed-wing aircraft and are complicated by the nonlinear and unsteady aerodynamics, as well as thruster dynamics and other nonlinear effects like the propeller slipstream etc., which become dominant during maneuvering flight.

Many works in the literature rely upon system identification (ID) techniques to identify models (input-to-output transfer functions) of agile UAVs in maneuvering flight, since the test data required for ID can be gathered relatively easily for these small, inexpensive, and readily available off-the-shelf UAVs. The test data may be acquired from extensive flight tests [1], wind-tunnel tests [2], and even through motion tracking [3]. Unfortunately, system ID methods lack generality and require extensive testing to cover the complete flight envelope of an aerobatic UAV.

Comprehensive physics-based models that cover the full flight envelope of agile UAVs are scarce in literature. This is not surprising since most works on autonomous control of agile UAVs are limited to specific maneuvers and as such the flight dynamics are determined either via system ID discussed above, or by first principles that simplify drastically for the specific maneuver. Green *et al.* [4], for instance, models the dynamics of a small fixed-wing MAV in hover maneuver using first principles. The model is simplified due to the absence of nonlinear or unsteady aerodynamics in that particular maneuver. A more detailed treatment is carried out in [5] for the hover and transition (cruise-to-hover or vice versa) of small fixed-wing UAVs. Also, agile UAVs in hover/ perch or transition maneuvers closely resemble vertical takeoff

Waqas Khan is a Ph.D. candidate in the Dept. of Mechanical Engineering, McGill University, Montreal, QC, Canada (phone: +1 514-560-3637; e-mail: waqas.khan@mail.mcgill.ca).

Meyer Nahon is a Professor in the Dept. of Mechanical Engineering, McGill University, Montreal, QC, Canada (email: meyer.nahon@mcgill.ca).

and landing (VTOL) aircraft, also called tail-sitters, and as such benefit from the standard modeling techniques for VTOLs, see [6], for these particular maneuvers. Stone [7] presents a nonlinear dynamics model for his wing-in-propeller-slipstream tail-sitter UAV. To a large extent, the model is physics-based i.e. based on 6-dof rigid body equations of motion with aerodynamic and thruster forces/ moments, and propeller slipstream effect. Another work for VTOL UAV is by Roy *et al.* [8].

The most relevant work is by Selig [9] that aims to model maneuvering capabilities of small fixed-wing UAVs as realistically as possible through first principles. This comprehensive work models the aerodynamics for the full angle of attack and sideslip range, and takes into account various effects present during maneuvering flight. The dynamics model is integrated into the framework of a commercial simulator FS One, and though Ref. [9] provides some insight to the underlying dynamics and operation, it does not allow further development and use in path/ maneuver planning, trajectory generation or controller development.

The primary objective of this work is to present a dynamics model for agile UAVs that captures their behavior reasonably well for their entire working envelope covering conventional flight, high angle of attack flight, aerobatics and extreme maneuvers. The presented model is much simpler than the commercial FS One simulator and does not need tuning/ refinement as it does not include any semi-empirical factors. The model is implemented in a MATLAB/ Simulink simulation, setup to run both offline as well as a real-time simulator with the pilot-in-loop. The latter may serve as a platform for path/ motion planning including maneuver construction, trajectory generation as well as controller development to fulfil the long-term goal of autonomous aerobatic capabilities of agile UAVs.

II. KINEMATICS AND DYNAMICS

In this section, kinematics and rigid-body dynamics equations are presented that form the framework of the high-fidelity simulation for agile UAVs.

A. Reference Frames and Aircraft States

Two reference frames (body and inertial) are used to define the motion of the agile UAV. The body frame (superscript *B*) is defined as per the convention for fixed-wing aircraft: the origin is placed at the aircraft center of gravity (c.g.); the *x* axis is along the fuselage and points out of the nose; *y* axis is along the wing and points out of the starboard wing (right side of the airplane when viewed from rear); and *z* axis points down from the belly of the aircraft. Although the inertial frame can be any arbitrary fixed reference frame, it is quite common to choose the earth North-East-Down (NED) frame as the inertial frame. The origin is fixed at any point on the surface of the earth, e.g. starting point of the flight; the x^I axis points in the North direction, y^I points in the East direction, and z^I points vertically downwards towards the earth's center.

At any instance, the body and inertial frames can be related by a translation plus rotation transformation, implying that quantities in one frame can be easily expressed in the other frame. With quaternion attitude representation, the rotation transformation from the body to inertial frame is given as:

$$\Re_B^I = \begin{bmatrix} e_0^2 + e_1^2 - e_2^2 - e_3^2 & 2(e_1 e_2 - e_0 e_3) & 2(e_1 e_3 + e_0 e_2) \\ 2(e_1 e_2 + e_0 e_3) & e_0^2 + e_2^2 - e_1^2 - e_3^2 & 2(e_2 e_3 - e_0 e_1) \\ 2(e_1 e_3 - e_0 e_2) & 2(e_2 e_3 + e_0 e_1) & e_0^2 + e_3^2 - e_1^2 - e_2^2 \end{bmatrix} \quad (1)$$

The vice versa transformation from the inertial to the body frame is simply the transpose of the above rotation matrix $\Re_I^B = (\Re_B^I)^T$. The four-parameter quaternion representation $e = e_0 + e_1 \mathbf{i}^I + e_2 \mathbf{j}^I + e_3 \mathbf{k}^I$ is chosen for the agile UAV's attitude, where the first element e_0 is the scalar part defining the angle of rotation, while the other three elements (e_1, e_2 and e_3) define the unit vector of the axis of rotation in the inertial frame. For a proper rotation, the quaternion must be a unit quaternion, i.e. $\|e\| = \sqrt{e_0^2 + e_1^2 + e_2^2 + e_3^2} = 1$.

The Euler angle representation (roll ϕ, pitch θ, and yaw ψ), which is widely used for conventional fixed-wing UAVs, is not suitable for agile UAVs since it suffers a mathematical singularity at $\theta = \pm 90$ deg. where it fails to distinguish between roll and yaw. However, since Euler angles are intuitive and easy to visualize, it is frequently required to transform the quaternion to Euler angles and vice versa. These transformation relationships can be found in the literature [10].

In assembling the equations of motion, thirteen state variables are introduced. These are the: 1) three North-East-Down position states $\mathbf{p}^I = [p_N, p_E, p_D]^T$ in the inertial frame, 2) three translation velocity states $\mathbf{V}_{cg}^B = [u, v, w]^T$ in the body frame (also called body velocity), 3) four angular position states $e = [e_0, e_1, e_2, e_3]^T$ for aircraft attitude, and 4) three angular velocity states $\mathbf{\Omega}^B = [p, q, r]^T$ in the body frame (also called body rates).

B. Kinematics and Rigid Body Dynamics Equations

The 13-state, 6-dof equations of motion can be found in any aircraft text book, see e.g. [10].

$$\begin{bmatrix} \dot{p}_N \\ \dot{p}_E \\ \dot{p}_D \end{bmatrix} = \begin{bmatrix} e_0^2 + e_1^2 - e_2^2 - e_3^2 & 2(e_1 e_2 - e_0 e_3) & 2(e_1 e_3 + e_0 e_2) \\ 2(e_1 e_2 + e_0 e_3) & e_0^2 + e_2^2 - e_1^2 - e_3^2 & 2(e_2 e_3 - e_0 e_1) \\ 2(e_1 e_3 - e_0 e_2) & 2(e_2 e_3 + e_0 e_1) & e_0^2 + e_3^2 - e_1^2 - e_2^2 \end{bmatrix} \begin{bmatrix} u \\ v \\ w \end{bmatrix}$$

$$\begin{bmatrix} \dot{u} \\ \dot{v} \\ \dot{w} \end{bmatrix} = \begin{bmatrix} rv - qw \\ pw - ru \\ qu - pv \end{bmatrix} + g \begin{bmatrix} 2(e_1 e_3 - e_0 e_2) \\ 2(e_2 e_3 + e_0 e_1) \\ e_0^2 + e_3^2 - e_1^2 - e_2^2 \end{bmatrix} + \frac{1}{m} \left(\mathbf{F}_{aero}^B + \mathbf{F}_{thr}^B \right)$$

$$\begin{bmatrix} \dot{e}_0 \\ \dot{e}_1 \\ \dot{e}_2 \\ \dot{e}_3 \end{bmatrix} = \frac{1}{2} \begin{bmatrix} \lambda(1 - \|e\|^2) & -p & -q & -r \\ p & \lambda(1 - \|e\|^2) & r & -q \\ q & -r & \lambda(1 - \|e\|^2) & p \\ r & q & -p & \lambda(1 - \|e\|^2) \end{bmatrix} \begin{bmatrix} e_0 \\ e_1 \\ e_2 \\ e_3 \end{bmatrix} \quad (2)$$

$$\begin{bmatrix} \dot{p} \\ \dot{q} \\ \dot{r} \end{bmatrix} = (\mathbf{I})^{-1} \left(\begin{bmatrix} (I_y - I_z)qr + I_{xz}pq \\ (I_z - I_x)pr + I_{xz}(r^2 - p^2) \\ (I_x - I_y)pq - I_{xz}qr \end{bmatrix} + \mathbf{M}_{aero}^B + \mathbf{M}_{thr}^B \right)$$

where the aircraft mass and inertia tensor is represented by *m* and $\mathbf{I}$ respectively. In the quaternion propagation of Eq. (2), the diagonal term $\lambda(1 - \|e\|^2)$ is a cost minimizing function that tries to maintain $\|e\| = 1$ so that the resulting quaternion always represents a proper rotation. A value of $\lambda = 1000$ is deemed to work well in Ref. [10], but may be tuned depending
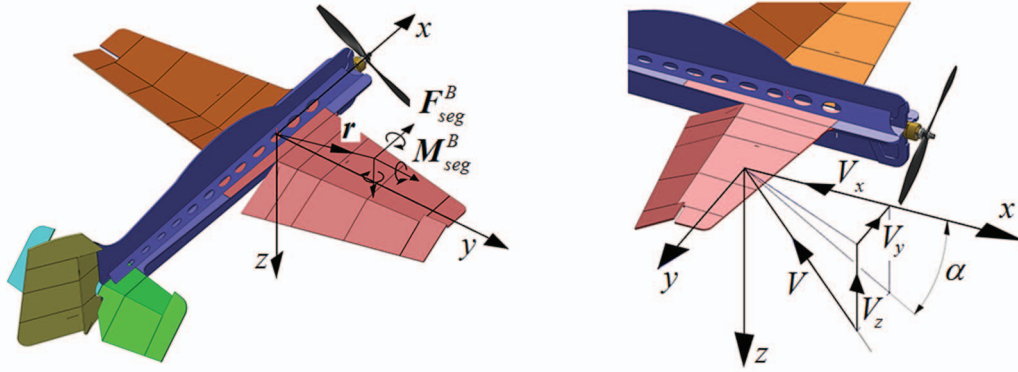
Figure 2.   Decomposition of YAK54 (left), and segment velcoity and angle of attack (right).

on the solved used. The aerodynamic force and moment ($\boldsymbol{F}_{aero}^{B}$ and $\boldsymbol{M}_{aero}^{B}$) and thruster force and moment ($\boldsymbol{F}_{thr}^{B}$ and $\boldsymbol{M}_{thr}^{B}$) acting on the aircraft frame are evaluated in Secs. III and IV A respectively.

Equation (2) is implemented in Simulink for the test platform discussed in Sec. V A. A variable time-step Runge-Kutta integrator (ODE45) is used to propagate the equation.

III.   AERODYNAMICS

The challenging task of modeling agile UAV aerodynamics includes modeling:

- full flight envelope i.e. ±180 deg. angle of attack and sideslip range,

- partial flow conditions over the aerodynamic surfaces, e.g. in the case of a partially stalled wing,

- low aspect ratio surfaces ($AR \simeq 1.5$ - 4) operating at low Reynolds numbers (20,000 to 150,000),

- big control surfaces (up to 50% flap-to-chord ratios) and deflections (up to 50 deg.),

- realistic phenomena (adverse yaw, induced roll etc.),

- aerodynamic interaction between aircraft components such as wing, tail etc., and

- unsteady aerodynamic effects particularly during rapid maneuvering.

In the present work, the aerodynamics model for agile UAVs is based on a component breakdown approach as it can be used to easily model aerodynamic surfaces in detail [9, 11]. A discussion on the component breakdown approach follows in the next section. A mathematically simple aerodynamics model is presented herein to facilitate real-time implementation of the UAV simulation.

A. Component Breakdown Approach

The component breakdown approach, also known as strip theory, requires the decomposition of the aircraft components (wing, tail etc.) into a number of segments each producing lift, drag and moment about its aerodynamic center (a.c.). Their forces and moments are transferred to the aircraft c.g. using kinematics and summed up to give the total aerodynamic force and moment acting on the aircraft. The decomposition process

allows us to model each segment independently with its own aerodynamics, as well as the possibility of modeling almost every geometric detail of the individual segment. This means, for example, that some segments can be modeled with different velocity due to the propwash over them, some segments may be modeled as 100% control surfaces while others can be partial control surfaces, and so on.

Figure 2 shows the decomposition of the YAK54 test platform. The segments are defined keeping in view the aircraft geometry and other constraints like propwash etc. For example, the starboard wing is divided into seven segments such that the first three segments from the wing root lie within the propeller slipstream. More so, the first segment at the wing root has no control surface, while the last segment at the tip has a different configuration with an aileron horn. Similarly, segments can be defined on all components of the aircraft. They, based on their geometry and flow conditions, will produce aerodynamic forces and moments about their a.c.

1. Segment Velocity and Angle of Attack

To determine the flow conditions of each aircraft segment, its velocity is calculated at its a.c. using kinematics and appropriate contributions of propwash, wind etc.

$$\boldsymbol{V} = \boldsymbol{V}_{cg}^{B} + \boldsymbol{\Omega}^{B} \times \boldsymbol{r} + \boldsymbol{V}_{S} + \boldsymbol{V}_{ind} + \boldsymbol{V}_{QS} + \boldsymbol{V}_{wind} \qquad (3)$$

The first two terms come from the translation and rotation of the aircraft defined by the body velocity $\boldsymbol{V}_{cg}^{B}$ and body rate $\boldsymbol{\Omega}^{B}$ respectively. The position vector $\boldsymbol{r} = [r_x, r_y, r_z]^T$ is from the aircraft c.g. to the aerodynamic center of the segment, measured in the body frame.

The velocity $\boldsymbol{V}_{S}$ due to the propeller slipstream is calculated for each segment at its a.c. using the slipstream model in Sec. IV B. The induced velocity $\boldsymbol{V}_{ind}$ on the segment due to aerodynamic interference from other segments is also considered using the Biot-Savart law [6]. This is particularly important for the vertical and horizontal tail segments which have considerable downwash from the upstream wing segments. External wind contribution is also added to Eq. (3).

Furthermore, the maneuvers performed by agile UAVs are quite rapid, and hence unsteady aerodynamic effects on the segment must be considered. From the works in the literature [3, 9], it is concluded that even aggressive maneuvers like hover, blender etc. may be reasonably modeled using quasi-steady aerodynamics i.e. time-dependent unsteady effects may

be neglected but other effects due to the rate of change of angle of attack $\dot{\alpha}$, and change in down velocity $\dot{h}$ (plunging) must be considered. The quasi-steady effect of plunging is already accounted for when using Eq. (3), while for the effect of $\dot{\alpha}$, the velocity perturbation $V_{QS} = 0.5\dot{\alpha}c\,\mathbf{k}$ [12] is explicitly added in Eq. (3). A detailed discussion on the unsteady aerodynamics follows in Sec. III D.

The angle of attack of each segment is calculated from its velocity. For segments on the horizontal surfaces (see Fig. 2), the angle of attack is:

$$\alpha = \operatorname{atan}2(V_z, V_x) - \alpha_0 \qquad (4)$$

A similar expression can be written for the vertical surfaces for which the angle of attack is measured between y and x velocity components. The geometric zero-lift angle α_0 is included so that the angle of attack is measured from the zero-lift line. For symmetric airfoils like the flat plates in Fig. 2, $\alpha_0 = 0$.

It is assumed that the aerodynamic contribution of the spanwise velocity component is negligible. This means that the y direction flow for horizontal surfaces like wing etc., and the z direction flow for vertical surfaces like rudder etc., produce only friction drag and is thus neglected. Depending on the angle of attack of each segment, its aerodynamics can fall either in the low-alpha regime or in the high-alpha regime, discussed later in Secs. III B and C respectively.

2. Segment Forces and Moments
The aerodynamic forces and moments on each horizontal segment are written as:

$$\begin{aligned}
\mathbf{F}_{seg}^B &= 0.5\rho bc V_{xz}^2 \left[CF_{seg,x}, 0, CF_{seg,z} \right]^T \\
\mathbf{M}_{seg}^B &= 0.5\rho bc^2 V_{xz}^2 \left[0, C_{M,ac}, 0 \right]^T
\end{aligned} \qquad (5)$$

Again, a similar expression may be written for vertical segments. Here b and c are the span and mean aerodynamic chord (m.a.c.) of the segment. The segment's force coefficients are obtained from its lift and drag coefficients:

$$\begin{aligned}
CF_{seg,x} &= C_L \sin\alpha - C_D \cos\alpha \\
CF_{seg,y} &= CF_{seg,z} = -C_L \cos\alpha - C_D \sin\alpha
\end{aligned} \qquad (6)$$

The quasi-steady aerodynamic coefficients C_L, C_D, and $C_{M,ac}$ are determined in the next sections, depending on whether the segment under consideration is in the low-alpha or high-alpha regime, with corrections for aspect ratio and control surface deflection. When considering time-dependent unsteady effects (see Sec. III D), dynamic coefficients C_L^{dyn}, C_D^{dyn} and $C_{M,ac}^{dyn}$ may be used in Eq. (6) above.

3. Total Aerodynamic Force and Moment
The forces and moments obtained for each segment via Eq. (5) above, are transferred to the aircraft c.g. using kinematics, and added as follows:

$$\begin{aligned}
\mathbf{F}_{aero}^B &= \Sigma \mathbf{F}_{seg}^B \\
\mathbf{M}_{aero}^B &= \Sigma \left(\mathbf{M}_{seg}^B + \mathbf{r} \times \mathbf{F}_{seg}^B \right)
\end{aligned} \qquad (7)$$

Equation (7) represents the net aerodynamic force and moment acting at the aircraft c.g. and is used in the equations of motion.

B. Low-Alpha Aerodynamics
In the current work, low-alpha aerodynamics refer to the aerodynamics that exist up to the point where the flow starts separating from the leading-edge with no reattachment downstream. As such the complex stall phenomenon is included in the low-alpha regime.

In the linear range, the lift, drag and moment coefficients may be calculated using the vast airfoil data available in the literature, or standard equations [13]:

$$\begin{aligned}
C_L &= C_{L\alpha}\alpha \\
C_D &= C_{d,0} + C_L^2 / \pi k_{ost} AR \\
C_{M,ac} &= -\text{const}.
\end{aligned} \qquad (8)$$

where α is measured from the zero-lift line, $C_{L\alpha}$ is the lift-curve slope of a finite surface, $C_{d,0}$ is the drag coefficient due to skin friction (usually 0.02 to 0.04), k_{ost} is the Ostwald's efficiency factor (typically 0.85 - 0.9). The moment at the aerodynamic center is negative (i.e. pitch down) and constant in the linear region. For thin flat plates, the a.c. and the center of pressure are coincident and hence $C_{M,ac} = 0$ [13].

The aerodynamic coefficients in Eq. (8) are influenced by a number of factors including airfoil shape, aspect ratio, Reynolds number, Mach number, control surface deflections, and unsteady flow conditions. For the range of operational speeds of agile UAVs, Reynolds number and Mach number have little effect on the aerodynamic performance [10, 14]. The effect of other factors however are considered.

1. Effect of Low Aspect Ratio
Agile UAVs are designed to keep most of the aerodynamic and control surfaces immersed in the propwash to maintain lift and control under zero/ low forward speed flight and extreme maneuvers, wherein the external flow is largely detached from the surfaces. Consequently, the aerodynamic and control surfaces of agile UAVs end up being low aspect ratio, typically 1.5 to 4.

The effect of aspect ratio to reduce lift and increase drag is well-known [13], and can be accounted for by decreasing the lift-curve slope, for which several expressions are available in the literature. Presently, the expression given in [6] is used:

$$C_{L\alpha} = C_{l\alpha}\left(\frac{AR}{AR + 2(AR+4)/(AR+2)} \right) \qquad (9)$$

Where $C_{l\alpha}$ is the 2D lift-curve slope and may be taken as 2π for thin flat plates. According to Ref. [13], the various expressions for the lift-curve slope agree within a few percent.

Special attention is required when the aspect ratio is below 2, and/or if the airfoil sections are thin with sharp leading and side edges. This is because as the aspect ratio gets lower, the side (tip) vortices engulf more and more of the upper surface as shown in Fig. 3 (a). Additionally, if the leading-edge is sharp, flow separation from the leading-edge and consequently leading-edge vortices (LEVs) will form with increasing angle of attack. In the low-alpha regime, both the leading-edge and
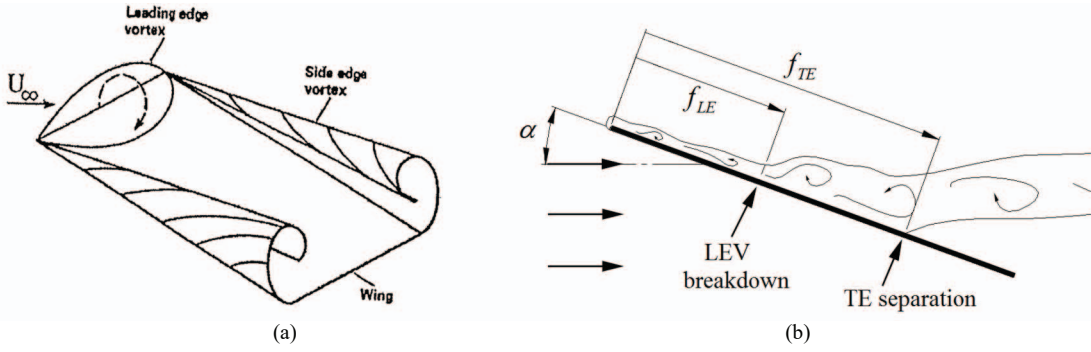
Figure 3. (a) Leading and side-edge vortices, and (b) leading-edge vortex breakdown and trailing-edge separation.

side-edge vortices essentially reattach on the upper surface of the wing, see Fig. 3 (a), further reducing pressure there, and thus give rise to an additional vortex lift.

The total lift for a LAR wing is therefore the sum of potential and vortex lifts. The former may be calculated using potential flow theories such as the Prandtl's lifting line theory, while an expression for the later for delta wings was proposed by Polhamus [15] using the leading-edge suction analogy. Later, Lamar [16] extended Polhamus' theory to other non-delta planforms with sharp leading and side edges, using the suction analogy for side-edge vortices as well. Recent experimental investigations in relation to MAVs [14, 17] thoroughly discuss the effect of low aspect ratio surfaces, and show that the mathematical expressions given by Polhamus and Lamar agree well with experimental data.

Hence if the agile UAV has thin aerodynamic surfaces with sharp leading and side edges, see e.g. Fig. 1, and/or the aspect ratios are low (≤ 2), Eq. (8) is not well suited; instead the nonlinear equations for the lift, drag and moment coefficients given by Polhamus and Lamar are used:

$$C_L = C_{L,p} + C_{L,v} = K_p \sin\alpha\cos^2\alpha + K_v \sin^2\alpha\cos\alpha$$
$$C_D = C_{d,0} + C_L \tan\alpha = C_{d,0} + K_p \sin^2\alpha\cos\alpha + K_v \sin^3\alpha \quad (10)$$
$$C_{M,ac} = -(x_p - 0.25)K_p \sin\alpha\cos\alpha - (x_e - 0.25)K_v \sin^2\alpha$$

The potential (linear) and vortex (nonlinear) lift contributions are represented by the coefficients $C_{L,p}$ and $C_{L,v}$, and parameters K_p and K_v. For LAR rectangular surfaces, $K_p = C_{L\alpha}$ [13]. The vortex lift comes from both the leading and side edges, represented by parameters $K_{v,LE}$ and $K_{v,SE}$ respectively. While these individual parameters also vary with aspect ratio, the total vortex lift parameter $K_v = K_{v,LE} + K_{v,SE}$ remains nearly constant, within $\pm 10\%$ of π [16], and therefore $K_v = \pi$ in this work.

In the pitching moment coefficient of Eq. (10), x_p and x_e represent the normalized chordwise locations of the potential and vortex lifts respectively. For rectangular flat plate surfaces, the center of pressure for potential lift is at quarter-chord location i.e. $x_p = 0.25$, while x_e is determined from the experimental results of [14] to be nearly constant at 0.42.

2. Effect of Stall
The low-alpha regime is extended to cover the stall phenomenon by including the effect of trailing-edge separation and leading-edge vortex breakdown. These stall mechanisms are briefly discussed below.

a) Trailing-Edge Separation
The conventional mechanism for stalling is the progressive separation of flow from the upper surface starting from the trailing-edge. This causes the loss of lift associated with the stall phenomenon. The normalized chordwise location of the TE separation is represented by f_{TE} as shown in Fig. 3 (b), such that for fully attached flow $f_{TE} = 1$. As the angle of attack increases, f_{TE} decreases and becomes zero for fully separated flow at the LE, i.e. at the start of high-alpha regime.

b) Leading-Edge Vortex Breakdown
A thin wing with sharp leading-edge is also characterized by the formation of LE vortices that reattach and travel along the upper surface of the wing. However, at a certain distance downstream of the leading-edge, these LEVs breakdown due to turbulence etc., thereby causing a loss in the vortex lift. The normalized chordwise position of the LEV breakdown is represented by f_{LE} as shown in Fig. 3 (b). At low angles of attack, the LEV breakdown down occurs at the trailing-edge (i.e. $f_{LE} = 1$); as the angle of attack increases f_{LE} starts to decrease and becomes zero at higher angles of attack with the LEV breakdown occurring at the leading-edge.

c) Aerodynamic Coefficients
For thin airfoils with sharp leading-edge, both the TE separation and LEV breakdown are responsible for loss in lift during stall. Following the work of Goman et al. [18], the following equation is proposed which expands the low-alpha regime equation (10) to cover the stall phenomenon:

$$C_L = 0.25\left(1+\sqrt{f_{TE}}\right)^2\left(K_p\sin\alpha\cos^2\alpha + f_{LE}^2 K_v \sin^2\alpha\cos\alpha\right)$$
$$C_D = C_{d,0} + C_L\tan\alpha \quad (11)$$
$$C_{M,ac} = -0.0625\left(-1+6\sqrt{f_{TE}}-5f_{TE}\right)K_p\sin\alpha\cos^2\alpha$$
$$+ f_{LE}^2 K_v \sin^2\alpha\cos\alpha$$

From Eq. (11), the LEV breakdown affects only the vortex lift, but the TE separation affects the total lift. Under quasi-steady condition f_{TE} and f_{LE} depend upon α and $\dot\alpha$, and may be written from [18, 19] as:

$$f_{TE} = 0.5\left[1 - \tanh\left\{a_{TE}\left(\alpha - \tau_{TE}\dot\alpha - \alpha_{TE}\right)\right\}\right]$$
$$f_{LE} = 0.5\left[1 - \tanh\left\{a_{LE}\left(\alpha - \tau_{LE}\dot\alpha - \alpha_{LE}\right)\right\}\right] \quad (12)$$

The semi-empirical coefficients (a_{LE}, a_{TE}, α_{LE} and α_{TE}) may be determined from static data available in the literature. Table I lists the semi-empirical coefficients for rectangular flat plates of various aspect ratios obtained by curve fitting Eq. (11) to

1307

TABLE I. SEMI-EMPIRICAL COEFFICIENTS FOR FLAT PLATES

AR	a_{LE}	a_{TE}	α_{LE}	α_{TE}	$\alpha_{high,S}$
0.167	3	5.9	59	59	49
0.333	3.64	15.51	58.6	58.6	54
0.5	4.48	32.57	58.2	58.2	56
0.75	7.18	39.44	50	51.85	48
1	10.2	48.22	41.53	41.46	40
1.25	13.38	59.29	26.7	28.09	29
1.5	14.84	21.55	23.44	39.4	27
1.75	14.49	7.74	21	35.86	25
2	9.95	7.05	18.63	26.76	24
3	12.93	5.26	14.28	19.76	22
4	15	6.5	11.6	16.43	22
6	15	6.5	10	14	20

static lift coefficient data taken from Refs. [14, 17]. The quasi-steady time constants τ_{LE} and τ_{TE} however must be determined from dynamic test data.

3. Effect of Control Surface Deflection

In the low-alpha regime, the general effect of control surface deflection is to change the camber of an airfoil and shift the lift curve. By convention, a positive deflection increases the camber and shifts the curve upwards. To account for flap deflection, an effective angle of attack $\alpha' = \alpha - \alpha_0'$ is used in Eq. (11). The effective zero-lift angle of attack α_0' due to flap deflection is obtained by solving the nonlinear equation:

$$-K_p \sin\alpha_0' \cos^2\alpha_0' + f_{LE}^2 K_v \sin^2\alpha_0' \cos\alpha_0' = \frac{\Delta C_L}{0.25\left(1+\sqrt{f_{TE}}\right)^2} \quad (13)$$

The increase in lift coefficient due to flap deflection is given as $\Delta C_L = C_{L\alpha}\tau_f\eta_f\delta_f$ [13], see Fig. 4, where the flap effectiveness factor τ_f and empirical factor η_f is found from [13] for a given flap-to-chord ratio and flap deflection. On top of being simple, there are two advantages of the above proposed method: 1) it accounts for the effect of aspect ratio through the $C_{L\alpha}$ term, and 2) it is valid for deflections as large as 70 deg. Also, the change in the stall angle due to flap deflection is accounted for using the method given in [13].

C. High-Alpha Aerodynamics

The high-alpha regime starts when the flow is completely separated from the upper surface starting from the leading-edge with no reattachment downstream. This occurs at an angle of attack $\alpha_{high,S}$ corresponding to $f_{TE} = 0$. Thereafter, the airfoil profile has negligible effect and it acts as a flat plate for which the aerodynamic coefficients may be calculated using flat plate theory or expressions presented by Hoerner et al. [20], or Leishman [12].

1. Effect of Aspect Ratio

Though all expressions correlate to the experimental data very well, the expression by Hoerner et al. [20] is used in the current work since a correction for aspect ratio has been made to this expression by Lindenburg [21]. Accordingly, the normal force coefficient for finite AR flat plate is given by:

$$C_N = C_{d,90}\sin\alpha\left[\frac{1}{0.56+0.44\sin\alpha} - 0.41\left\{1-\exp\left(\frac{-17}{AR}\right)\right\}\right] \quad (14)$$

The lift, drag and moment coefficients are then written as:

$$C_L = C_N\cos\alpha - C_A\sin\alpha$$
$$C_D = C_N\sin\alpha + C_A\cos\alpha \quad (15)$$
$$C_{M,ac} = -C_N\left[0.25 - 0.175(1-2\alpha/\pi)\right]$$

The 2D drag coefficient $C_{d,90}$ of a flat plate normal to flow has a typical value of 1.98, while the axial force coefficient $C_A = 0.5C_{d,0}\cos\alpha$ [21]. The pitching moment coefficient equation is also taken from [21] and is found to fit well for high angles of attack.

2. Effect of Control Surface Deflection

No analytical or experimental is found in the literature for the effect of control surface deflection at high angles of attack. Therefore, a simple but effective approach is proposed in the current work to account for control surface deflection in the high-alpha regime.

It was pointed out that after complete separation of the flow from the upper surface, an airfoil behaves like a flat plate. Keeping this in view, it is proposed that an airfoil with a positive flap deflection in the high-alpha regime is also equivalent to a flat plate, see Fig. 5, but with a higher drag coefficient $C_{d,90}'$ and at a higher effective angle of attack $\alpha' = \alpha + \alpha_f$. From geometry $\alpha_f = a\sin\left[(c_f/c')\sin\delta_f\right]$ and $c' = \sqrt{(c-c_f)^2 + c_f^2 + 2c_f(c-c_f)\cos\delta_f}$. For a positive deflection, α_f will also be positive.

The 2D drag coefficient of the "equivalent" flat plate (normal to flow) changes as the airfoil becomes convex or concave to the flow depending on whether the deflection is positive or negative. A qualitative estimate of drag for 2D shapes is given in Ref. [13]. The 2D drag coefficient for a 90 deg. concave is 2.2, for a flat plate is 1.98, and for a 90 deg. convex is 1.55. A segment of the agile UAV is limited by the maximum possible deflection, and thus may, at most, form a 50 deg. convex or concave to the flow. In lieu of this, the data from [13] is curve-fitted to predict $C_{d,90}'$ for other deflections:

$$C_{d,90}' = -0.00426\delta_f^2 + 0.21\delta_f + 1.98 \quad (16)$$

For a positive 50 deg. deflection, the airfoil becomes concave for which Eq. (16) gives $C_{d,90}' = 2.1$, while for a negative 50 deg. deflection, the airfoil becomes convex with $C_{d,90}' = 1.8$. For zero deflection, the 2D drag coefficient attains the standard value of 1.98 for a flat plate normal to flow.
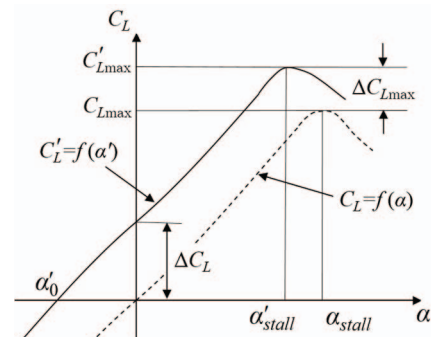

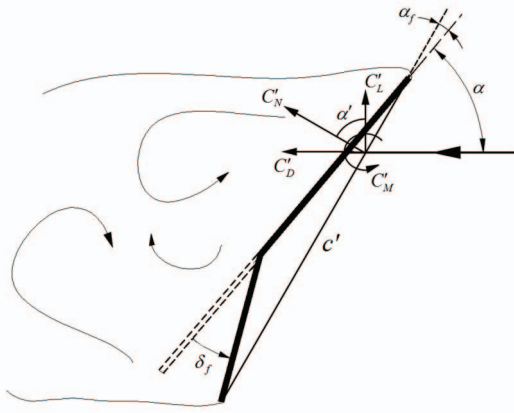Figure 4.   Effect of control surface deflection in the low-alpha regime.

1308

Figure 5. Effect of control surface deflection in the high-alpha regime.

D. Unsteady Aerodynamics

Some of the impressive aerobatic maneuvers performed by agile UAVs are very rapid and therefore it seems only appropriate to consider the time-dependent unsteady aerodynamic contributions in achieving these maneuvers. Essentially, unsteady aerodynamics come into play with sudden changes in the aircraft motion that are fast enough so that the flow does not have sufficient time to adjust to the motion, leading to unsteady manifestations such as apparent mass, circulatory, and dynamic stall effects.

It is particularly useful to characterize the degree of unsteadiness during maneuvering flight. This is done by the reduced frequency parameter which for agile UAV segments, may be defined based on their rate of change of angle of attack i.e. $k_r = \dot{\alpha}c/2V$. According to [12], $k_r = 0$ represents steady flow, $0 < k_r \leq 0.05$ represents quasi-steady flow i.e. the time dependent effects are small enough to be neglected, and $k_r > 0.05$ represents unsteady flow for which time dependent effects become dominant and must be considered. For agile UAVs with an average chord of 0.3 m and an average cruise speed of 5 m/s, a maneuver must produce at least $\dot{\alpha} \simeq 100$ deg./s in order to be unsteady. Even with the most dynamic maneuvers like blender and snap, it is difficult to achieve such high rates in the angle of attack. Thus most maneuvers of agile UAVs do not qualify as unsteady and may be dealt with the quasi-steady treatment presented in the previous sections. This conclusion is consistent with the experimental observations of Refs. [3, 9].

Several models exist in the literature to account for the unsteady aerodynamic effects including the well-known Beddoes-Leishman, Risø, and Larsen models. Unfortunately, their formulation is not suitable for the current work since they are unable to take into account the previously obtained quasi-steady aerodynamic curves which pre-include the effect of low AR and control surface deflection. Therefore, with the help of existing models, an unsteady aerodynamics suitable for agile UAVs is presented here.

The four main time dependent effects that must be included are: 1) added mass, 2) circulatory response, 3) dynamic TE separation, and 4) dynamic LEV breakdown. The first two effects pertain to attached flow condition, while the latter two are for stalled flow condition.

1. Attached Flow Condition ($f_{TE} = 1$)

Added Mass: Added mass (also called apparent mass) effect arises when the fluid surrounding the segment is suddenly accelerated along with it. The effect may be modeled as added mass terms to account for the reaction forces required to accelerate the fluid mass. From [22], the increase in lift and moment coefficient due to added mass effect may be given as:

$$C_L^{AM} = \frac{\pi c}{2V^2}\left[V\dot{\alpha} + \ddot{h} + \frac{1}{4}c\ddot{\alpha}\right]$$
$$C_{M,ac}^{AM} = -\frac{\pi c}{2V^2}\left[\frac{1}{4}\ddot{h} + \frac{3}{32}c\ddot{\alpha}\right] \tag{17}$$

The above equation has been simplified for the pitching axis located at the segment's aerodynamic center.

Circulatory Response: The time varying wake shed from the airfoil induces downwash and affects circulation, leading to an overall delayed response to a change of angle of attack. The classical unsteady model of Theodorsen accounts for this effect by multiplying the quasi-steady lift and moment with the Theodorsen transfer function, see [12]. The original Theodorsen formulation assumed pure harmonic motion of the airfoil and is extended to the entire complex plane by using a generalized Theodorsen function $C(\bar{s})$, where $\bar{s} = (c/2V)s$. Thus from [22],

$$C_L^{circ} = C_L C(\bar{s})$$
$$C_{M,ac}^{circ} = 2C_{M,ac} \tag{18}$$

For the pitching axis location other than the a.c., the moment expression would contain an additional term multiplied with $C(\bar{s})$, see [12]. The two pole approximation for $C(\bar{s})$ given in [12] is used here:

$$C(\bar{s}) \simeq \frac{0.5\bar{s}^2 + 0.2808\bar{s} + 0.01365}{\bar{s}^2 + 0.3455\bar{s} + 0.01365} \tag{19}$$

Equation (19) represents two first-order differential equations, thereby introducing two additional states into the overall simulation.

Total Unsteady Response: Under attached flow condition, the total unsteady response is the sum of added mass and circulatory terms.

$$C_L^{dyn} = C_L^{AM} + C_L^{circ}$$
$$C_D^{dyn} = C_{d,0} + C_L^{dyn}\tan\alpha \tag{20}$$
$$C_{M,ac}^{dyn} = C_{M,ac}^{AM} + C_{M,ac}^{circ}$$

2. Stalled Flow Condition ($0 \leq f_{TE} < 1$)

For unsteady flow conditions, the chordwise locations of TE separation and LEV breakdown become time-dependent and represented via first order differential equations [18, 19]:

$$\tau_{TE,1}\dot{f}_{TE}^{dyn} + f_{TE}^{dyn} = 0.5\left[1 - \tanh\left\{a_{TE}\left(\alpha - \tau_{TE,2}\dot{\alpha} - \alpha_{TE}\right)\right\}\right]$$
$$\tau_{LE,1}\dot{f}_{LE}^{dyn} + f_{LE}^{dyn} = 0.5\left[1 - \tanh\left\{a_{LE}\left(\alpha - \tau_{LE,1}\dot{\alpha} - \alpha_{LE}\right)\right\}\right] \tag{21}$$

Again the time constants $\tau_{LE,1}$, $\tau_{LE,2}$, $\tau_{TE,1}$, and $\tau_{TE,2}$ must be determined from dynamic test data of the airfoil.

1309

Total Unsteady Response: Under stalled flow conditions aerodynamic coefficients (C_L^{dyn}, C_D^{dyn} and $C_{M,ac}^{dyn}$) are determined from Eq. (11) but using dynamic TE separation (f_{TE}^{dyn}) and LEV breakdown (f_{LE}^{dyn}) locations given by Eq. (21) above instead of quasi-steady ones given by Eq. (12).

IV. THRUSTER DYNAMICS AND PROPELLER SLIPSTREAM EFFECTS

A. Thruster Dynamics

An agile UAV is typically equipped with a propeller driven thruster to achieve high thrust-to-weight ratio, around 2-3, enabling it to perform thrust-borne maneuvers wherein most or all of the UAV's weight is supported by the thruster rather than the lift of its wings. Furthermore, in maneuvering flight, the thruster on the agile UAV is subjected to varying flow conditions during flight. The thruster may become stationary i.e. not moving forward such as during a hover maneuver. The thruster may experience pure axial flow i.e. flow aligned with its rotation axis like that encountered during level flight or vertical takeoff. The thruster may encounter oblique flow i.e. flow at an angle to its rotation axis. Such a situation arises, for example, during aerobatics and even during random wind gusts. Finally, the thruster may also experience reverse flow as a result of a maneuver. Under these various flow conditions, the thruster generates different aerodynamic thrust and torque and may even generate other secondary forces and moments which can contribute significantly to the agile UAV dynamics.

A thruster model for general forward flight conditions of small UAVs is presented by the authors in Refs. [23, 24]. It models the sub-components namely the battery, brushless DC (BLDC) motor, and propeller, as well the gyroscopic effect in-detail. As such, the model is able to predict the six-axis thruster forces and moments under both steady-state and dynamic (transient) conditions.

The battery and BLDC motor parts of the model are embedded directly into the UAV simulation, but the propeller part is iterative, and therefore it is run offline for the test platform thruster to generate propeller maps that are saved as loop-up tables in the UAV simulation. The propeller part of the model is run for advance ratios $J = 0$ to 1, and propeller tilt angles $\varphi_p = 0$ to 90 deg. The resulting propeller's aerodynamic force and moment coefficients, $CF_p, CM_p = f(J, \varphi_p)$ are stored as look-up tables called the propeller maps. During simulation, the velocity V_p at the propeller disc center due to translation and rotation of the aircraft is calculated using Eq. (3), while the propeller's rotational speed n (in rev/s) is given by the motor model. The advance ratio $J = V_p/nD_p$, and propeller tilt angle $\varphi_p = \operatorname{atan}(V_{p,yz}/V_{p,x})$ are calculated, and the coefficients are looked up from the stored table against these values. Then the propeller's aerodynamic force and moment are calculated using $F_p = \rho n^2 D_p^4 CF_p$ and $M_p = \rho n^2 D_p^5 CM_p$.

For rearward flight of the aircraft e.g. a tail-slide maneuver, the propeller operates in the vortex ring state as the rearward speed is not too high for stability reasons. Other states (turbulent wake and windmill brake) that require high

rearward speeds are unlikely to be encountered during controlled maneuvers of the UAV. All these states have been studied much for helicopter rotors in descent flight, wherein a mathematical treatment may be found for these, see e.g. [12].

Although a slight drop and fluctuations in thrust (from static value) are associated with the vortex ring state [12], these are small and neglected. Hence in the current work, the thrust and torque coefficient ($CF_{p,x}$ and $CM_{p,x}$) in the vortex ring state are assumed to remain constant at their static ($J = 0$) value. Also, from the experimental results of Theys *et al.* [25], it is assumed that the secondary propeller forces and moments ($CF_{p,y}$, $CF_{p,z}$, $CM_{p,y}$, and $CM_{p,z}$) in vortex ring state have the same value as in forward flight.

Finally, the thruster force and moment may be written as:

$$
\begin{aligned}
\boldsymbol{F}_{thr} &= \boldsymbol{F}_p^B \\
\boldsymbol{M}_{thr} &= [-(I_{thr,R}\dot{\omega} + \tau_{damp}), 0, 0]^T + \boldsymbol{M}_p^B + \boldsymbol{M}_{gyro}
\end{aligned}
\tag{22}
$$

The thruster force is solely due to the propeller (expressed in the body frame), whereas the thruster moment is due to the motor, propeller and gyroscopic effects. In the above equation, $I_{thr,R}$ is the rotational inertia of all moving parts of thruster, ω is the propeller rotational speed in rad/s, and τ_{damp} is the torque required to overcome magnetic damping in the motor. Refer to [23, 24] for further details.

B. Propeller Slipstream Effects

Another key aerodynamic component that must be modeled in detail for agile UAVs is the propeller slipstream produced by the thruster, since it provides additional airflow over the aircraft's surfaces, allowing the aircraft to maintain lift and control during near-zero forward speed flight like that encountered during vertical takeoff and landing, as well as during aerobatic maneuvers wherein the external flow is largely detached from the aircraft's control surfaces. Lift and control under these conditions is achieved primarily by immersing the UAV's aerodynamic and control surfaces, entirely or partially, in its propeller slipstream, thereby keeping the surfaces effective at all times. Hence detailed knowledge of the slipstream velocity is essential to accurately determine the aerodynamic and control forces/ moments.

1. Axial Slipstream Velocity

For axial velocity, a novel slipstream model for small UAVs have been presented by the authors in Ref. [26]. It takes into account both the acceleration and diffusion phenomenon occurring within the slipstream, and hence it is able to predict the axial slipstream velocity reasonably well up to 6 propeller diameters downstream, which is sufficient for most small sized UAVs. More so, the model matches the simplicity of conventional models like the momentum theory, and is therefore implemented directly in the UAV simulation. The inputs to the model are propeller's rotational speed n and thrust coefficient $F_{p,x}$, and its output is the slipstream velocity V_S at each segment's aerodynamic center, given its location.

For rearward flight of the agile UAV, the axial velocity is calculated using the slipstream model above as long as the rearward speed is low (< 20% of the induced velocity at hover), because the axial velocity is still able to reach the aircraft surfaces. But as the rearward speed increases beyond

1310

this, the axial slipstream velocity is counteracted completely by the external reverse flow and it is unable to reach the aircraft surfaces. Then V_S is taken to be zero.

2. Swirl Slipstream Velocity

The swirl velocity is not modeled explicitly; rather its effect on the agile UAV is considered. Manu effects of swirl velocity are documented [27], but these are small and neglected. Only the main effect of swirl to reduce the thruster reaction moment is included in the simulation as follows.

The swirl velocity gives rise to a positive rolling moment on the aircraft as it causes downwash on the starboard surfaces and upwash on the port surfaces. Further, the swirl flow coiling clockwise around the fuselage adds to this effect. The positive rolling moment due to swirl counteracts some of the negative rolling moment exerted by the thruster on the airframe. This effect of swirl is modeled by reducing $M_{thr,x}$ to 40% of its value for a typical aerobatic UAV configuration [28]. For rearward flight, the above mentioned reduction to $M_{thr,x}$ is done as long as the rearward speed low (< 20% of the induced velocity at hover). At higher rearward speeds, the swirl velocity is unable to impinge upon the aircraft surfaces and hence no reduction is done to $M_{thr,x}$.

V. VALIDATION

Extensive validation of the model has been done through wind-tunnel tests, static bench tests, and pilot-in-loop simulations, and the model is found to be sufficiently accurate. Herein, simulated results of some maneuvers flown by the pilot are presented as a final overall validation.

A. Test Platform

The test platform chosen is the *YAK54 Electric 3D Aerobat* - an off-the-shelf high performance RC plane, see Fig. 1. It has three control surfaces (ailerons, elevator, and rudder) and a powerful thruster unit.

The mass of the ready-to-fly test platform was measured to be 465 g. The YAK54 thruster unit produces a maximum thrust of 9.9 N, resulting in a thrust-to-weight ratio of around 2.17. The inertial parameters and c.g. location (measured from the propeller plane) were evaluated from a detailed CAD model of the YAK54 made in SolidWorks. Therefore, $I_x =$ 2.45E-3 kg.m², $I_y =$ 2.07E-2 kg.m², $I_z =$ 2.25E-2 kg.m², $I_{xz} =$ 1.7E-4 kg.m², and $x_{cg} =$ -0.293 m, $y_{cg} =$ 0 m, and $z_{cg} =$ 0.007 m.

The peak deflections are: ±50 deg. for the ailerons, ±40 deg. for the elevator and ±60 deg. for the rudder. The sign convention for control surface deflection follows the standard for fixed-wing aircraft i.e. a positive deflection gives corresponding negative moment [13].

B. Real-Time Pilot-in-Loop Simulations

The model was implemented in a real-time simulator with the pilot-in-loop. A professional RC pilot who has experience flying the actual YAK54 test platform, tested the simulator by flying various RC maneuvers including harrier, hover, knife-edge etc. His overall comments were that the simulation behaves much like the real aircraft. Figures 6 and 7 show two maneuvers flown by the pilot in the simulator (data recorded at 100 Hz). Pilot inputs are plotted in terms of control surface deflections and thruster's rpm. The trajectory of the aircraft is shown by the colored line; the color represents progression of time (blue = start and red = end). The aircraft is drawn (scale = 1.7 times actual size) after every 0.8 s.

Shown in Fig. 6 is a knife-edge maneuver. At around $y = -$40 m, the pilot enters into a knife-edge maneuver which is characterized by a roll angle of 90 deg. During the maneuver, the UAV nose is kept pitch-up using the rudder, and the aircraft weight is supported by thrust's vertical component (and not by the wing lift). After $y = -50$ m, the pilot gives a ramp elevator command, creating a tightening knife-edge spiral. The aircraft is also allowed to lose some altitude by not increasing the thrust (to compensate for increased drag due to elevator).

A more dynamic maneuver called a blender/ inverted spin is flown by the pilot in the simulation as shown in Fig. 7. The pilot starts by nose diving the aircraft (i.e. 90 deg. pitch down). As the aircraft nose dives, a maximum right aileron input is given to start a fast roll. A positive elevator and rudder commands are given instantaneously (and maintained) so that the tremendous momentum along the roll direction gets
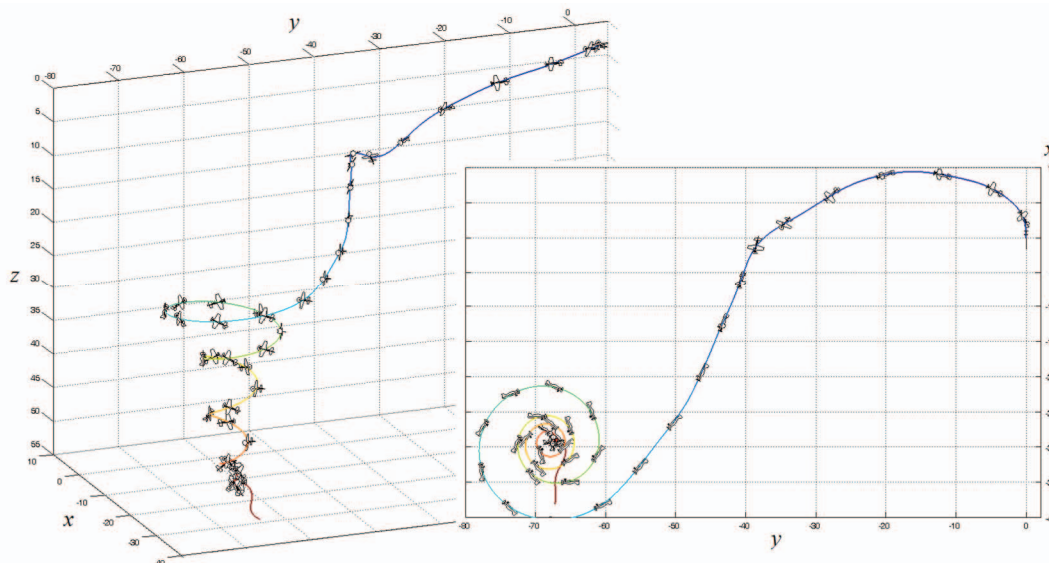

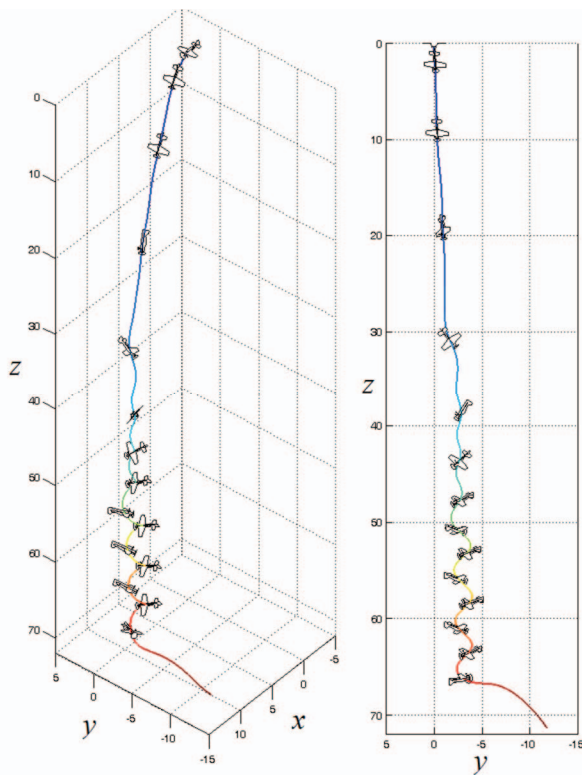Figure 6.   Knife-edge spiral maneuver flown by the pilot in simulation.

Figure 7.   Blender/ inverted spin flown by the pilot in simulation.

transferred to the yaw direction. Thereafter, the UAV spins inverted in a tight circle while slowly coming down, and the overall effect is dramatic. To exit the maneuver, the pilot relieves the elevator and rudder, and increases thrust to tangent out of the maneuver.

VI.   CONCLUSION

In this paper we have presented a 6-dof dynamics model for agile UAVs capable of predicting their behavior for the full flight envelope covering conventional flight, high angle of attack flight, and extreme aerobatics and maneuvers. Nonlinear post-stall and unsteady aerodynamics, thruster dynamics and propeller slipstream effects have all been taken into account through first principles. A thorough validation of the model has been done via wind-tunnel tests, static bench tests, and pilot-in-loop simulations. The real-time implementation of the model with the pilot-in-loop and hardware-in-loop will serve as a useful platform for path/ motion planning including maneuver construction, trajectory generation as well as controller development to fulfil the long-term goal of autonomous aerobatic capabilities of agile UAVs.

REFERENCES

[1]   B. Johnson, and R. Lind, "High Angle-of-Attack Flight Dynamics of Small UAVs," AIAA Paper 2009-61, Jan. 2009.

[2]   D. Kubo, K. Maraoka, and N. Okada, "High Angle of Attack Flight Characteristics of a Wing-In-Propeller-Slipstream Aircraft," presented at the 27th Int. Congress of the Aeronautical Sciences, Nice, France, Sept. 2010.

[3]   R. Cory, and R. Tedrake, "Experiments in Fixed-Wing UAV Perching," AIAA Paper 2008-7256, Aug. 2008.

[4]   W. E. Green, and P. Y. Oh, "A Hybrid MAV for Ingress and Egress of Urban Environments," *IEEE Trans. Robotics*, vol. 25, no. 2, pp. 253-263, April 2009.

[5]   K. J. Krogh, "Developing a Framework for Control of Agile Aircraft Platforms in Autonomous Hover," M. S. Thesis, Dept. Aeronautics and Astronautics, Univ. of Washington, Washington, USA, 2009.

[6]   B. W. McCormick, *Aerodynamics of V/STOL Flight*, New York: Dover, 1999.

[7]   R. H. Stone, "Aerodynamic Modeling of the Wing-Propeller Interaction for a Tail-Sitter Unmanned Air Vehicle," *J. Aircraft*, vol. 45, no. 1, pp. 198-210, Jan-Feb. 2008.

[8]   S. Roy, A. Moreau, and M. Grosbois, "Modeling and Simulation of a Forward-Swept Wing, Vertical Takeoff or Landing & Thrust Vectored Remotely Piloted Vehicle," in *Proc. Canadian Aeronautics and Space Institute Annual General Meeting on Aircraft Design and Development Symposium*, Toronto, ON, 2007.

[9]   M. S. Selig, "Real-Time Flight Simulation of Highly Maneuverable Unmanned Aerial Vehicles," *J. Aircraft*, vol. 51, no. 6, pp. 1705-1725, Nov. 2014.

[10]   R. W. Beard, and T. W. McLain, *Small Unmanned Aircraft: Theory and Practice*, New Jersey: Princeton University Press, 2012.

[11]   W. Khan, and M. Nahon, "Real-Time Modeling of Agile Fixed-Wing UAV Aerodynamics," in *Proc. 2015 Int. Conf. on Unmanned Aircraft Systems*, Denver, CO, June 2015, pp. 1188-1195.

[12]   J. G. Leishman, *Principles of Helicopter Aerodynamics*, 2nd ed., Cambridge: Cambridge University Press, 2006.

[13]   B. W. McCormick, *Aerodynamics, Aeronautics and Flight Mechanics*, 2nd ed., New York: Wiley, 1995.

[14]   G. E. Torres, "Aerodynamics of Low Aspect Ratio Wings at Low Reynolds Numbers With Applications to Micro Air Vehicle Design," Ph. D. Dissertation, Dept. Aerospace and Mech. Eng., Univ. of Notre Dame, IN, 2002.

[15]   E. C. Polhamus, "Predictions of Vortex-Lift Characteristics by a Leading-Edge-Suction Analogy," *J. Aircraft*, vol. 8, no. 4, pp. 193-199, April 1971.

[16]   J. E. Lamar, "Extension of Leading-Edge-Suction Analogy to Wings with Separated Flow around the Side Edges at Subsonic Speeds," NASA TR R-428, 1974.

[17]   M. Okamoto, and A. Azuma, "Aerodynamic Characteristics at Low Reynolds Numbers for Wings of Various Planforms," *AIAA Journal*, vol. 49, no. 6, pp. 1135-1150, June 2011.

[18]   M. Goman, and A. Khrabrov, "State-Space Representation of Aerodynamic Characteristics of an Aircraft at High Angles of Attack," *J. Aircraft*, vol. 31, no. 5, pp. 1109-1115, Sept-Oct.1994.

[19]   D. Fischenberg, and R. V. Jategaonkar, "Identification of Aircraft Stall Behavior from Flight Test Data," RTO MP-11 Paper No. 17, March 1999.

[20]   S. F. Hoerner, and H. V. Borst, *Fluid-Dynamic Lift: Practical Information on Aerodynamic and Hydrodynamic Lift*, 2nd ed., 1985. Ch. 5, 17, 21.

[21]   C. Lindenburg, "Stall Coefficients," presented at the *IEA Symposium on the Aerodynamics of Wind Turbines*, NREL, CO, Dec. 4-5, 2010.

[22]   D. H. Hodges, and G. A. Pierce, *Introduction to Structural Dynamics and Aeroelasticity*, Cambridge: Cambridge University Press, 2002, pp. 201-206.

[23]   W. Khan, and M. Nahon, "Toward an Accurate Physics-Based UAV Thruster Model," *IEEE/ASME Trans. Mechatronics*, vol. 18, no. 4, pp. 1269-1279, Aug. 2013.

[24]   W. Khan, and M. Nahon, "A Propeller Model for General Forward Flight Conditions," *Int. J. of Intelligent Unmanned Systems*, vol. 3, no. 2/3, pp. 72-92, 2015.

[25]   B. Theys, G. Dimitriadis, T. Andrianne, P. Hendrick and J. De Schutter, "Wind Tunnel Testing of a VTOL MAV Propeller in Tilted Operating Mode," in *Proc. 2014 Int. Conf. on Unmanned Aircraft Systems*, Orlando, FL, 2014, pp. 1064-1072.

[26]   W. Khan, and M. Nahon, "Development and Validation of a Propeller Slipstream Model for Unmanned Aerial Vehicles," *J. Aircraft*, vol. 52, no. 6, pp. 1985-1994, Nov-Dec. 2015.

[27]   G. K. Ananda, R. W. Deters, and M. S. Selig, "Propeller-Induced Flow Effects on Wings of Varying Aspect Ratio at Low Reynolds Numbers," AIAA Paper 2014-2152, June 2014.

[28]   M. S. Selig, "Modeling Propeller Aerodynamics and Slipstream Effects on Small UAVs in Realtime," AIAA Paper 2010-7938, Aug. 2010.